

# The hypernuclear chart

E. Khan,<sup>1</sup> J. Margueron,<sup>2</sup> F. Gulminelli,<sup>3</sup> and Ad. R. Raduta<sup>4</sup>

<sup>1</sup>*Institut de Physique Nucléaire, Université Paris-Sud, IN2P3-CNRS, F-91406 Orsay cédex, France*

<sup>2</sup>*Institut de Physique Nucléaire de Lyon, Université Claude Bernard Lyon 1, IN2P3-CNRS, F-69622 Villeurbanne cédex, France*

<sup>3</sup>*CNRS/ENSICAEN/LPC/Université de Caen Basse Normandie, UMR6534, F-14050 Caen cédex, France*

<sup>4</sup>*IFIN-HH, Bucharest-Magurele, POB-MG6, Romania*

(Dated: May 5, 2022)

**Background:** A large number of hypernuclei, where a considerable fraction of nucleons is replaced by  $\Lambda$  hyperons, is expected to be bound. However the hypernuclear landscape remains largely unknown, at least from a microscopic point of view.

**Purpose:** We calculate the comprehensive hypernuclear chart for even-even hypernuclei with magic numbers of  $\Lambda$ 's (for  $Z \leq 120$  and  $\Lambda \leq 70$ ) and estimate the number of bound systems, considering the present uncertainties in the  $\Lambda$ -nucleon and  $\Lambda$ - $\Lambda$  interactions.

**Method:** We consider a density functional approach adjusted to microscopic Brueckner-Hartree-Fock calculations, where the  $\Lambda\Lambda$  term is corrected in a phenomenological way, to reproduce present experimental constraints. Different models which strongly deviate at large densities, but giving the same bond energy, are generated in order to take into account the uncertainties related to the high density equation of state.

**Results:** The number of bound even-even hypernuclei is estimated to  $491680 \pm 34400$ . This relatively low uncertainty is due to the fact that the well constrained low density and highly unconstrained high density behavior of the energy functional turn out to be largely decoupled. Results in hypernuclei appear to be almost independent of the choice for the high-density part of the  $\Lambda\Lambda$  interaction. The location of the hyperdriplines is also evaluated. Significant deviations from Iron-Nickel elements can be found for hypernuclei with the largest binding energy per baryon. Proton, neutron and hyperon magicity evolution and triple magic hypernuclei are studied. Possible bubbles and haloes effect in hypernuclei are also discussed.

**Conclusions:** The present results provide a first microscopic evaluation of the hypernuclear landscape. They shall benefit from the more and more accurate design of the  $\Lambda$ -based functionals. The measurements of  $\Lambda$  and multi- $\Lambda$  hypernuclei would greatly help to provide such critical information.

PACS numbers: 21.80.+a, 21.60.Jz, 21.10.Dr

## I. INTRODUCTION

The study of the hypernuclei structure is currently generating a large interest [1–3], especially with dedicated experimental programs such as J-Parc in Japan or PANDA at FAIR. Present facilities can only produce single and double  $\Lambda$  hypernuclei in a limited domain of mass. However, a general understanding of the specificity of hypernuclear structure with respect to nuclear structure requires the evaluation of the global hypernuclear chart, with strangeness as the third dimension [4, 5]. Several microscopic models have been devoted to the calculation of hypernuclei [1–3, 6–18]. It is therefore timely to draw the landscape of the hypernuclear chart, based on a microscopic approach. Some recent works [2, 3] address this problem within phenomenological mean field models. However, the uncertainties on the hypernuclear chart associated to the choice of the functional in the strangeness sector are difficult to evaluate, since present experimental data on hypernuclei are scarce, and therefore a large arbitrariness is associated to the modelization of the hyperonic energy functional. To minimize such uncertainties, it is important to use as much as possible microscopically founded energy functionals from Brueckner or Dirac-Brueckner calculations as well as the few available experimental data. The present work is an attempt towards that direction.

The regular nuclear landscape, including an estimation of the uncertainties on its limits defined by the drip-lines, has

been only recently microscopically studied [19], owing to the growth of calculation capacities. This is also due to the recent use of evaluation methods [20, 21] for the uncertainties generated by the only input of such microscopic calculations: the nucleon-nucleon (NN) energy functional. The resulting uncertainty on the number of bound nuclei is typically of the order of 7% [19].

The present work aims to generalize such a study by designing the limits of the hypernuclear landscape, and evaluating the uncertainties associated with the  $\Lambda$ -nucleon ( $\Lambda N$ ) and the  $\Lambda\Lambda$  functionals. For this purpose fully microscopic calculations of nuclei and hypernuclei are performed using the energy density functional approach. We use a Skyrme functional optimized on nuclear physics data for the NN channel, while  $\Lambda N$  and  $\Lambda\Lambda$  functionals fitted on microscopic Brueckner-Hartree-Fock (BHF) calculations are used, with modifications in order to take into account hypernuclei data constraints.

Section II details the energy density functional used, focusing on the way to design the  $\Lambda\Lambda$  component. Section III is devoted to the determination of the corresponding parameters of the  $\Lambda\Lambda$  functional. The Hartree-Fock calculations for hypernuclei are performed in Section IV. Since in the hyperonic channel the spin-orbit interaction is expected to be very weak [22], the hypernuclear charts, location of the hyperdriplines and the estimation of the number of bound even-even hypernuclei are evaluated for hypernuclear number  $\Lambda=0, 2, 8, 20, 40$  and 70. In Section V, the gross properties of

hypernuclear structure are analyzed, namely the evolution of the energy per baryon as a function of the  $\Lambda N$  and  $\Lambda\Lambda$  functionals. A study of magicity evolution in hypernuclei, as well as of possible bubbles and haloes effects is also undertaken. Finally, Appendix A details the link between the bond energy and the  $\Lambda\Lambda$  functional whereas Appendix B provides an update of the strangeness analog resonances in multihyperons hypernuclei.

## II. DENSITY FUNCTIONAL THEORY FOR HYPER-NUCLEAR MATTER AND HYPER-NUCLEI

We consider a non-relativistic system composed of interacting nucleons  $N$  and lambdas  $\Lambda$ . The total Hamiltonian reads,

$$\hat{H} = \hat{T}_N + \hat{T}_\Lambda + \hat{H}_{NN} + \hat{H}_{\Lambda\Lambda} + \hat{H}_{N\Lambda}, \quad (1)$$

where  $\hat{T}_A$  is the kinetic energy operator and  $\hat{H}_{AB}$  the interaction operator acting between  $A$  and  $B$  ( $=N$  and  $\Lambda$ ). We work in the mean-field approximation where the ground state of the system is given by the tensor product,  $|\Phi_N\rangle \otimes |\Phi_\Lambda\rangle$ , where  $|\Phi_N\rangle = \Pi_i a_i^+ |-\rangle$  is a Slater determinant of nucleon states and  $|\Phi_\Lambda\rangle = \Pi_\lambda a_\lambda^+ |-\rangle$  is a Slater determinant of lambda states. The total Hamiltonian (1) can be expressed in terms of the nucleons ( $i$ ) and lambda ( $\lambda$ ) states as,

$$\hat{H} = \sum_i \hat{t}_i + \sum_\lambda \hat{t}_\lambda + \frac{1}{2} \sum_{i,j} \hat{v}_{ij}^{NN} + \frac{1}{2} \sum_{\lambda,\mu} \hat{v}_{\lambda\mu}^{\Lambda\Lambda} + \sum_{\lambda,i} \hat{v}_{i\lambda}^{N\Lambda}. \quad (2)$$

In the following, we will consider the density functional theory which allows relating in a direct way the BHF predictions for uniform matter to the properties of hyper-nuclei.

### A. Energy-density functional deduced from BHF

In the present study of hypernuclei and nuclear matter we use a density functional which has been determined directly from BHF theory including nucleons and hyperons [12, 13]. The total energy density  $\varepsilon(\rho_N, \rho_\Lambda)$  is related to the energy per particle calculated within the BHF framework,  $e_{BHF}$ , as  $\varepsilon(\rho_N, \rho_\Lambda) = (\rho_N + \rho_\Lambda)e_{BHF}(\rho_N, \rho_\Lambda)$  and is decomposed in different terms,

$$\varepsilon(\rho_N, \rho_\Lambda) = \frac{\hbar^2}{2m_N} \tau_N + \frac{\hbar^2}{2m_\Lambda} \tau_\Lambda + \varepsilon_{NN}(\rho_N) + \varepsilon_{N\Lambda}(\rho_N, \rho_\Lambda) + \varepsilon_{\Lambda\Lambda}(\rho_\Lambda), \quad (3)$$

where, in infinite nuclear matter, the kinetic energy densities  $\tau_N$  and  $\tau_\Lambda$  are simple functions of the matter density:  $\tau_i = \frac{3}{5}(6\pi^2/g_i)^{2/3} \rho_i^{5/3}$ , with  $g_i = 4(2)$  for  $i = N(\Lambda)$ .

In the nucleon sector, we use the SLy5 parametrization of the phenomenological Skyrme functional including non-local and spin-orbit terms, since it can correctly reproduce the properties of stable and exotic nuclei [23]. Concerning the strangeness sector, the spin-orbit interaction is known to be small [22], and is therefore neglected. The local density dependence of the  $N\Lambda$  component of the energy density,  $\varepsilon_{N\Lambda}(\rho_N, \rho_\Lambda)$ , is solely adjusted to the BHF predictions.

To pin down the  $N\Lambda$  coupling, the following energy density is defined:  $(\rho_N + \rho_\Lambda)e_{BHF}(\rho_N, \rho_\Lambda) - \rho_N e_{BHF}(\rho_N, 0) - \rho_\Lambda e_{BHF}(0, \rho_\Lambda)$ , where  $e_{BHF}(\rho_N, \rho_\Lambda)$  is the BHF energy per baryon in an infinite hyper-nuclear matter calculation. It is parameterized in terms of the nucleon and hyperon densities as [12, 13],

$$\varepsilon_{N\Lambda}(\rho_N, \rho_\Lambda) = -f_1(\rho_N)\rho_N\rho_\Lambda + f_2(\rho_N)\rho_N\rho_\Lambda^{5/3}, \quad (4)$$

where the first term physically corresponds to the attractive  $N\Lambda$  interaction, corrected by the presence of the medium given by the function  $f_1$ , and the second term is induced by the repulsive momentum dependent term of the  $\Lambda$  potential (considering the low-momentum quadratic approximation), also corrected by the medium through the function  $f_2$ . In the presence of the attractive  $\Lambda\Lambda$  interaction, the term  $\varepsilon_{\Lambda\Lambda}$  is solely determined by the hyperon density as [13],

$$\varepsilon_{\Lambda\Lambda}(\rho_\Lambda) = -f_3(\rho_\Lambda)\rho_\Lambda^2. \quad (5)$$

The functions  $f_i$  are given by the polynomial forms,

$$f_1(\rho_N) = \alpha_1 - \alpha_2\rho_N + \alpha_3\rho_N^2, \quad (6)$$

$$f_2(\rho_N) = \alpha_4 - \alpha_5\rho_N + \alpha_6\rho_N^2, \quad (7)$$

$$f_3(\rho_\Lambda) = \alpha_7 - \alpha_8\rho_\Lambda + \alpha_9\rho_\Lambda^2. \quad (8)$$

In principle, the functions  $f_1$  and  $f_2$  depend on the densities  $\rho_N$  and  $\rho_\Lambda$  associated to conserved charges in the medium. However, since nucleons are the dominant species, even in the presence of lambdas, the dependence on  $\rho_\Lambda$  is neglected in these functions. Concerning  $f_3$ , it trivially depends on  $\rho_\Lambda$  only, because it impacts the part of the functional referring to pure lambda matter.

Different  $N\Lambda$  potentials have been parameterized which equally well fit the scarce  $N\Lambda$  phase shifts, see for instance discussion and references in Ref. [24]. The present study is based on three of them for which a density functional has been derived, based on BHF predictions [12, 13], namely DF-NSC89, DF-NSC97a and DF-NSC97f. The functional DF-NSC89 is based on the Nijmegen soft-core potential NSC89 [25], while the functionals DF-NSC97a and DF-NSC97f are based on two of a series of six different hyperon-nucleon potentials which equally well reproduce the measured scattering lengths in the  $\Lambda N$  and  $\Sigma N$  channels, and correspond to different values of the magnetic vector meson ratio  $\alpha$  which cannot be constrained by the phase shift information [26, 27].

Although more recent functionals have been parameterized [24], by adding for instance isospin degree of freedom, the functionals considered in this study already represent a good sample of the uncertainty generated by the lack of empirical information in the strangeness sector. This affects microscopic approaches like BHF [12, 13, 15], although to a lesser extent than fully phenomenological mean field models [1–3, 6–11, 14, 16–18]. Indeed the models DF-NSC97a and DF-NSC97f correspond to the two extreme choices for the unconstrained  $\alpha$  parameter [26, 27], leading to the softest and stiffest equation of state, respectively. It should be noted that no experimental information is available on  $\Lambda$ - $\Lambda$  scattering, meaning that these phenomenological bare interactions are completely unconstrained in the  $\Lambda$ - $\Lambda$  channel. For

this reason, NSC89 does not contain any  $\Lambda$ - $\Lambda$  interaction. The NSC97 models assume for this channel a simple SU(3) extension of the original Nijmegen potential models to multiple strangeness  $S = -2$ . The values for the parameters  $\alpha_1 - \alpha_9$  of the functions  $f_1 - f_3$  are given in Table I for the functionals DF-NSC89, DF-NSC976a and DF-NSC97f.

The single particle energies in uniform matter are deduced from the energy functional (3), as  $e_N^{unif}(k) = \frac{\hbar^2 k^2}{2m_N} + v_N^{unif}$  and  $e_\Lambda^{unif}(k) = \frac{\hbar^2 k^2}{2m_\Lambda} + v_\Lambda^{unif}$ , where

$$v_N^{unif}(\rho_N, \rho_\Lambda) = v_N^{sky} + \frac{\partial \mathcal{E}_{N\Lambda}}{\partial \rho_N}, \quad (9)$$

$v_N^{sky}$  being deduced from the Skyrme functional [28, 29], and

$$v_\Lambda^{unif}(\rho_N, \rho_\Lambda) = \frac{\partial \mathcal{E}_{N\Lambda}}{\partial \rho_\Lambda} + \frac{\partial \mathcal{E}_{\Lambda\Lambda}}{\partial \rho_\Lambda}. \quad (10)$$

In the following, the hyperon potential  $v_\Lambda^{unif}$  is decomposed into two terms,  $v_\Lambda^{unif} = v_\Lambda^{(N),unif} + v_\Lambda^{(\Lambda),unif}$  using Eqs. (4) and (5),

$$v_\Lambda^{(N),unif} = \frac{\partial \mathcal{E}_{N\Lambda}}{\partial \rho_\Lambda} = -f_1(\rho_N)\rho_N + \frac{5}{3}f_2(\rho_N)\rho_N\rho_\Lambda^{2/3} \quad (11)$$

$$v_\Lambda^{(\Lambda),unif} = \frac{\partial \mathcal{E}_{\Lambda\Lambda}}{\partial \rho_\Lambda} = -2\alpha_7\rho_\Lambda + 3\alpha_8\rho_\Lambda^2 - 4\alpha_9\rho_\Lambda^3. \quad (12)$$

The term  $v_\Lambda^{(N),unif}$  stands for the contribution of the nucleons to the hyperon potential, while the term  $v_\Lambda^{(\Lambda),unif}$  represents the direct contribution of the hyperons to their own potential. The properties of the potential  $v_\Lambda^{(N),unif}$  are analyzed in Fig. 1 imposing  $\rho_n = \rho_p$ . On the left panel, the potential  $v_\Lambda^{(N),unif}$  is displayed without  $\Lambda$  particles, while on the right panel a small amount of  $\Lambda$  is considered, corresponding to a representative average  $\Lambda$ -density in single  $\Lambda$  hypernuclei (see Sec. III A). It is expected, from experimental single  $\Lambda$ -hypernuclei data, that the potential  $v_\Lambda^{(N)}$  is about -30 MeV at saturation density [12]. This empirical condition is satisfied for the three functionals DF-NSC89, DF-NSC97a and DF-NSC97f at saturation density, as shown on the left panel of Fig. 1. For a fixed and small amount of  $\Lambda$ , the potential  $v_\Lambda^{(N),unif}$  is attractive at large densities for all the functionals, due to the  $\alpha_3$  term in the function  $f_1$ . For a finite amount of  $\Lambda$ , the  $\alpha_6$  term in function  $f_2$  gives a repulsive contribution, and can compensate the attractive  $\alpha_3$  term if  $\rho_\Lambda > \left(\frac{3}{5}\frac{\alpha_3}{\alpha_6}\right)^{3/2}$ . For the functionals DF-NSC89, DF-NSC97a and DF-NSC97f, this occurs for  $\rho_\Lambda > 0.27, 0.09$  and  $0.15 \text{ fm}^{-3}$ , respectively. These substantially different numbers reveal the large uncertainties at high density in the predictions of the considered functionals.

The two terms  $v_\Lambda^{(N),unif}$  and  $v_\Lambda^{(\Lambda),unif}$  contributing to the potential  $v_\Lambda^{unif}$  (Eq. (10)) are compared in Fig. 2, as a function of the nucleonic density  $\rho_N$  and for different proportions of  $\Lambda$ . As expected, for a sufficiently large amount of  $\Lambda$ , the term

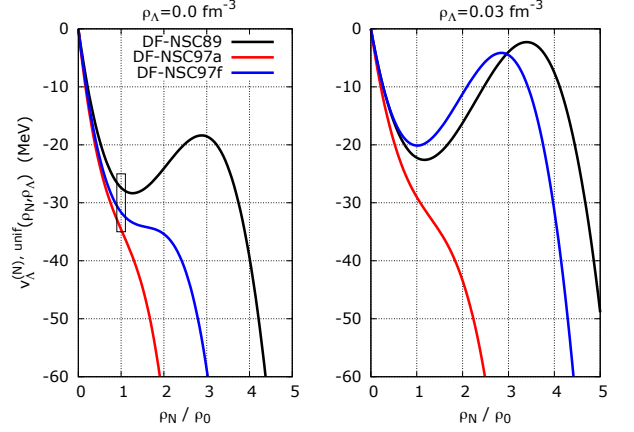


FIG. 1. (Color online) Potential  $v_\Lambda^{(N),unif}(\rho_N, \rho_\Lambda)$  as a function of the nucleon density  $\rho_N$  (in units of the saturation density  $\rho_0$ ) for the functionals DF-NSC89, DF-NSC97a and DF-NSC97f without  $\Lambda$  (left) and with  $\rho_\Lambda = 0.03 \text{ fm}^{-3}$  (right).

$v_\Lambda^{(N),unif}$  becomes repulsive at high nucleonic density. At low density the functionals DF-NSC97a and DF-NSC97f predict very close potentials  $v_\Lambda^{(\Lambda),unif}$ , but as the nucleonic density increases the predictions of these two functionals increasingly deviate. Since the dominant term in  $\alpha_9$  is attractive, the potential  $v_\Lambda^{(\Lambda),unif}$  will finally curve down at very high densities, but this occurs in physical situations which will be hardly met in nature. Indeed, for the functional DF-NSC97a, the potential continuously increases up to  $\rho_N \approx 10\rho_0$  and for a fraction of hyperons  $\leq 50\%$ . For DF-NSC97f, the effect of  $\alpha_9$  is already curving down the potential for  $\rho_N \approx 8\rho_0$  and 20% of  $\Lambda$ . In pure  $\Lambda$  matter, the potential  $v_\Lambda^{(\Lambda),unif}$  becomes repulsive between  $\rho_0/2$  and  $\rho_0$ . The functional DF-NSC97f predicts also a decreasing potential starting from  $1.5\rho_0$  while this behavior is pushed to much larger values (beyond  $20\rho_0$ ) with DF-NSC97a.

These differences between the functionals clearly show that the high density properties of hyper-matter are largely unconstrained. From the phenomenological point of view, the existence of very massive neutron stars (about  $2M_\odot$  [30]) requires a strongly repulsive  $v_\Lambda^{unif}$  potential at high density, which corresponds to a low value of the  $\alpha$  parameter, in terms of the elementary Nijmegen interactions. In principle, the very existence of such massive stars could be used as an extra constraint for the functional, and was often considered in the relativistic mean-field literature (see for instance the recent work [31] and Refs. therein). However, due to the presence of different hyperon species in the core of massive neutron stars, with highly unknown interaction couplings, it is not straightforward to convert this qualitative statement into a sharp constraint on the  $v_\Lambda^{unif}$  potential. More specifically, it should be noted that no BHF calculation is presently able to reproduce the empiri-

TABLE I. Parameters of the  $f_i$  functions, see Eqs. (6)-(8), for the functionals DF-NSC89, DF-NSC97a, DF-NSC97f.

Force	$\alpha_1$	$\alpha_2$	$\alpha_3$	$\alpha_4$	$\alpha_5$	$\alpha_6$	$\alpha_7$	$\alpha_8$	$\alpha_9$
DF-NSC89 [12, 13]	327	1159	1163	335	1102	1660	0	0	0
DF-NSC97a [13]	423	1899	3795	577	4017	11061	38	186	22
DF-NSC97f [13]	384	1473	1933	635	1829	4100	50	545	981

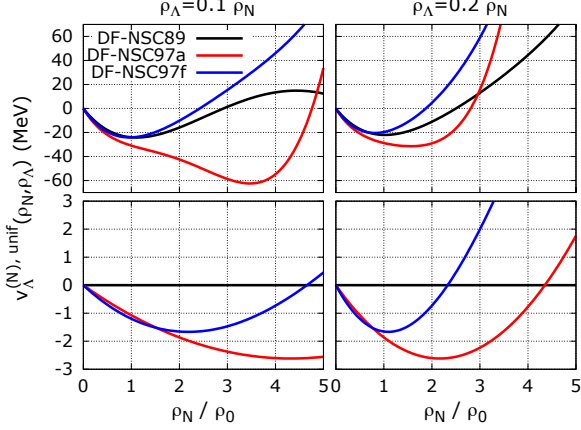


FIG. 2. (Color online) Comparison of  $v_{\Lambda}^{(N),unif}$  (top panels) and  $v_{\Lambda}^{(\Lambda),unif}$  (bottom panels), as a function of the nucleon density  $\rho_N$  (in units of the saturation density  $\rho_0$ ) for the functionals DF-NSC89, DF-NSC97a and DF-NSC97f and a  $\Lambda$  fraction set to 10% (left panels) and 20% (right panels).

cal observation of two solar mass neutrons stars. This contradiction between our knowledge of supra-nuclear matter and observation is usually called the hyperonization puzzle [32].

Finally, it can be noted from Fig. 2 that the  $v_{\Lambda}^{(\Lambda),unif}$  term is much smaller than  $v_{\Lambda}^{(N),unif}$ :  $v_{\Lambda}^{(\Lambda),unif}$  contributes to less than 10% to the total potential  $v_{\Lambda}^{unif}$ . In the functionals DF-NSC97a and DF-NSC97f, the contribution of the term  $v_{\Lambda}^{(\Lambda),unif}$ , induced by the  $\Lambda\Lambda$  interaction, to the properties of hyperonic matter is therefore expected to be rather weak. As discussed above, this result might not be entirely physical, since the  $\Lambda$ - $\Lambda$  interaction in the NSC97 models is not fitted on experimental data, but only extrapolated from the  $N - \Lambda$  interaction. The  $\Lambda\Lambda$  term of the functional can thus be phenomenologically adjusted as explained in the next section.

### B. Phenomenological correction to the term $\varepsilon_{\Lambda\Lambda}$

The term  $\varepsilon_{\Lambda\Lambda}$  defined by Eq. (5) is generated by the  $\Lambda\Lambda$  interaction: only the functionals DF-NSC97a and DF-NSC97f for which the  $\Lambda\Lambda$  interaction has been included in the BHF calculation, have a non-zero  $\varepsilon_{\Lambda\Lambda}$  [12, 13].

However, large uncertainties remain on the  $\Lambda\Lambda$  interaction,

as discussed above. The functionals introduced in section II A, based on an SU(3) extrapolation of the  $N - \Lambda$  bare interaction to the  $S = -2$  channel [25, 27], do not lead to a satisfactory description of the binding energy of double- $\Lambda$  hypernuclei [13], which is the only empirical information that we have on  $\Lambda - \Lambda$  couplings. [33–35]. Moreover, Fig. 2 shows that, though the DF-NSC97a and DF-NSC97f functionals in the  $\Lambda - \Lambda$  channel are very similar at low density, they drastically differ above saturation. In view of the already mentioned hyperonization puzzle, it is therefore reasonable to consider that an even larger uncertainty in the high density behavior has to be associated to the term  $\varepsilon_{\Lambda\Lambda}$ .

In the following, we therefore propose to modify the  $\varepsilon_{\Lambda\Lambda}$  term taking into account phenomenological arguments to deal with the uncertainty on the microscopic BHF results. In practice, the values of the  $\alpha_7, \alpha_8, \alpha_9$  parameters of the original functional (3) are replaced by different values  $\tilde{\alpha}_7, \tilde{\alpha}_8, \tilde{\alpha}_9$  defining the new  $\tilde{\varepsilon}_{\Lambda\Lambda}$  term,

$$\tilde{\varepsilon}_{\Lambda\Lambda} = -(\tilde{\alpha}_7 - \tilde{\alpha}_8 \rho_{\Lambda} + \tilde{\alpha}_9 \rho_{\Lambda}^2) \rho_{\Lambda}^2, \quad (13)$$

and the new potential  $\tilde{v}_{\Lambda}^{(\Lambda),unif}$ ,

$$\tilde{v}_{\Lambda}^{(\Lambda),unif} = -2\tilde{\alpha}_7 \rho_{\Lambda} + 3\tilde{\alpha}_8 \rho_{\Lambda}^2 - 4\tilde{\alpha}_9 \rho_{\Lambda}^3, \quad (14)$$

The determination of these parameters is based on the following phenomenological prescription:

- i) Since the  $\Lambda\Lambda$  interaction is expected to be repulsive at high density (to support for instance the observed  $2M_{\odot}$  neutron stars), the coefficient  $\tilde{\alpha}_9$  is taken as  $\leq 0$ .
- ii) A parameter  $x$  is introduced, which represents the  $\Lambda$  density (in units of the saturation density  $\rho_0$ ) where the  $\Lambda$  potential in hyperonic matter  $\tilde{v}_{\Lambda}^{(\Lambda),unif}$  (14) changes its sign and becomes repulsive.
- iii) Finally, we impose a relation between the  $\Lambda\Lambda$  interaction and the bond energy in  ${}^6\text{He}$ , obtained from the local density approximation, that we discuss hereafter [13].

Condition i) imposes  $\tilde{\alpha}_9 \leq 0$ . For convenience, we set  $\tilde{\alpha}_9 = 0$ , giving minimal repulsion. Fig. 2 shows that the contribution of the term  $\alpha_9$  appears at very high densities which are certainly never reached in neutron stars.

Condition ii) and Eq. (14) give

$$2\tilde{\alpha}_7 = 3\tilde{\alpha}_8 \rho_{\Lambda} = 3\tilde{\alpha}_8 x \rho_0, \quad (15)$$

meaning that the parameter  $x$  controls the high density behavior of  $\Lambda$  matter: the larger  $x$ , the softer the EoS with hyperons.

Condition iii) is related to the bond energy  $\Delta B_{\Lambda\Lambda}$  which is defined as [12, 13],

$$\Delta B_{\Lambda\Lambda}(A) = -E(A^{-2}Z) + 2E(A^{-1}Z) - E(A_{\Lambda\Lambda}Z), \quad (16)$$

where  $A^{-2}Z$  is a nucleus with no hyperon,  $A^{-1}Z$  is a single- $\Lambda$  hypernucleus, and  $A_{\Lambda\Lambda}Z$  is a double- $\Lambda$  hypernucleus. It should be noted that, experimentally,  ${}^6\text{He}$  and related hypernuclei provide the most accurate value of a bond energy with  $\Delta B_{\Lambda\Lambda} \simeq 1$  MeV [34, 35].

The relation between the bond energy and the functional is derived in Appendix A, providing

$$\Delta B_{\Lambda\Lambda}(A) \approx -2 \frac{\tilde{\epsilon}_{\Lambda\Lambda}(\rho_{\Lambda}(A))}{\rho_{\Lambda}(A)}. \quad (17)$$

Injecting Eq. (13) into Eq. (17), the following relation is deduced,

$$2\rho_{\Lambda}(A) \left[ \tilde{\alpha}_7 - \tilde{\alpha}_8 \rho_{\Lambda}(A) \right] = \Delta B_{\Lambda\Lambda}(A). \quad (18)$$

Using Eq. (15) and introducing  $x_{\Lambda}(A) = \rho_{\Lambda}(A)/\rho_0$ , the average  $\Lambda$ -density in double- $\Lambda$  hypernucleus  $A_{\Lambda\Lambda}Z$ , we obtain from Eq. (18),

$$\left[ 3x - 2x_{\Lambda}(A) \right] x_{\Lambda}(A) \rho_0^2 \tilde{\alpha}_8 = \Delta B_{\Lambda\Lambda}(A). \quad (19)$$

We can thus express the new parameters  $\tilde{\alpha}_7$  and  $\tilde{\alpha}_8$  as a function of  $x$ ,  $x_{\Lambda}(A)$  and  $\Delta B_{\Lambda\Lambda}(A)$ . from Eqs. (15) and (19) as,

$$\tilde{\alpha}_7 = \frac{3}{2} \frac{x \Delta B_{\Lambda\Lambda}(A)}{\left[ 3x - 2x_{\Lambda}(A) \right] x_{\Lambda}(A) \rho_0}, \quad (20)$$

$$\tilde{\alpha}_8 = \frac{\Delta B_{\Lambda\Lambda}(A)}{\left[ 3x - 2x_{\Lambda}(A) \right] x_{\Lambda}(A) \rho_0^2}. \quad (21)$$

The following expressions for the energy density and the potential are deduced from Eqs. (13) and (14):

$$\tilde{\epsilon}_{\Lambda\Lambda} = -\frac{\tilde{\alpha}_8}{2} \rho_{\Lambda}^2 (3x\rho_0 - 2\rho_{\Lambda}), \quad (22)$$

$$\tilde{v}_{\Lambda}^{(\Lambda),unif} = -3\tilde{\alpha}_8 \rho_{\Lambda} (x\rho_0 - \rho_{\Lambda}). \quad (23)$$

Since the parameters  $\tilde{\alpha}_7$  and  $\tilde{\alpha}_8$  are linearly related to the bond energy, the energy density  $\tilde{\epsilon}_{\Lambda\Lambda}$  also scales with the bond energy. The relation between  $\tilde{\alpha}_7$  and  $\tilde{\alpha}_8$  and the parameters  $x$  and  $x_{\Lambda}$  is more complicated. Let us consider the limit where  $x \gg x_{\Lambda}$ . In this case, the parameters  $\tilde{\alpha}_7$  and  $\tilde{\alpha}_8$  reduce to the simpler expressions:

$$\tilde{\alpha}_7^* = \frac{\Delta B_{\Lambda\Lambda}(A)}{2x_{\Lambda}(A)\rho_0} \quad \text{and} \quad \tilde{\alpha}_8^* = \frac{\Delta B_{\Lambda\Lambda}(A)}{3xx_{\Lambda}(A)\rho_0^2}. \quad (24)$$

It should be noted that  $\tilde{\alpha}_7^*$  is independent of  $x$  while  $\tilde{\alpha}_8^*$  is inversely related to  $x$ . Therefore the parameter  $\tilde{\alpha}_8$  is mostly related to the prescription ii), modifying the high density part of the mean field, while  $\tilde{\alpha}_7$  is almost independent of  $x$ . Moreover, at the limit  $x \gg x_{\Lambda}$ , the  $\Lambda$ -potential at the density  $\rho_{\Lambda}(A)$

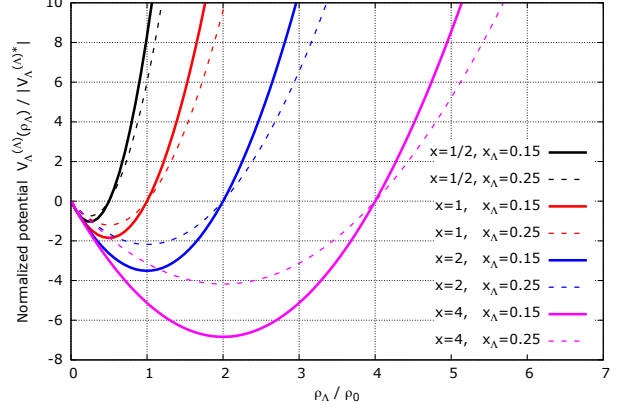


FIG. 3. (Color online) Normalized potential  $V_{\Lambda}^{(\Lambda)}(\rho_{\Lambda})/|V_{\Lambda}^{(\Lambda)*}|$  for several choices of  $x$  and  $x_{\Lambda}$ , see the caption.

is given by  $\tilde{v}_{\Lambda}^{(\Lambda)}(\rho_{\Lambda} = x_{\Lambda}(A)\rho_0) \approx \tilde{v}_{\Lambda}^{(\Lambda)*}$ , and the potential energy-density is given by  $\tilde{\epsilon}_{\Lambda\Lambda}(\rho_{\Lambda} = x_{\Lambda}(A)\rho_0) \approx \tilde{\epsilon}_{\Lambda\Lambda}^*$ , where

$$\tilde{v}_{\Lambda}^{(\Lambda)*} = -\Delta B_{\Lambda\Lambda}(A) \quad (25)$$

$$\tilde{\epsilon}_{\Lambda\Lambda}^* = -0.5\Delta B_{\Lambda\Lambda}(A)x_{\Lambda}(A)\rho_0. \quad (26)$$

The parameter  $\tilde{v}_{\Lambda}^{(\Lambda)*}$  is only related to the bond energy and is independent of  $x$  and  $x_{\Lambda}(A)$ , while the parameter  $\tilde{\epsilon}_{\Lambda\Lambda}^*$  depends only of the bond energy and  $x_{\Lambda}(A)$ , independently of the value of  $x$ . At the limit where  $x \gg x_{\Lambda}$ , the potential and the energy density at  $x_{\Lambda}(A)$  depends only of the bond energy and  $x_{\Lambda}(A)$ , and are independent of  $x$ . More generally, the following relations hold:

$$\frac{\tilde{v}_{\Lambda}^{(\Lambda)}(\rho_{\Lambda} = x_{\Lambda}(A)\rho_0)}{|\tilde{v}_{\Lambda}^{(\Lambda)*}|} = -1 + \frac{1}{3} \frac{x_{\Lambda}}{x} + o\left(\left(\frac{x_{\Lambda}}{x}\right)^2\right) \quad (27)$$

$$\frac{\tilde{\epsilon}_{\Lambda\Lambda}(\rho_{\Lambda} = x_{\Lambda}(A)\rho_0)}{|\tilde{\epsilon}_{\Lambda\Lambda}^*|} = -1 + o\left(\left(\frac{x_{\Lambda}}{x}\right)^2\right), \quad (28)$$

where the correction goes like  $x_{\Lambda}(A)/x$ .

Eqs. (27) and (28) show that the scaled  $\Lambda\Lambda$  potential  $\tilde{v}_{\Lambda}^{(\Lambda)}/\tilde{v}_{\Lambda}^{(\Lambda)*}$  and the scaled  $\Lambda$  energy  $\tilde{\epsilon}_{\Lambda\Lambda}/\tilde{\epsilon}_{\Lambda\Lambda}^*$  solely depend on  $x$  and  $x_{\Lambda}$ , and are independent of the bond energy. A complete representation of the parameter space can therefore be obtained by representing these scaled quantities as a function of the  $\Lambda$ -density, and largely varying only the two parameters  $x$  and  $x_{\Lambda}$ . These normalized potentials (respectively energies) are represented in Fig. 3 (respectively 4).

According to condition ii), the mean field potential changes its sign for the density  $\rho_{\Lambda} = x\rho_0$ . This is well observed in Fig. 3. Therefore, the effect of increasing the parameter  $x$  makes the  $\Lambda$ -mean field potential and energy density softer. In a similar but weaker way, Figs. 3 and 4 show that the effect of the parameter  $x_{\Lambda}$  is to soften the mean field potential and the energy density as  $x_{\Lambda}$  increases.

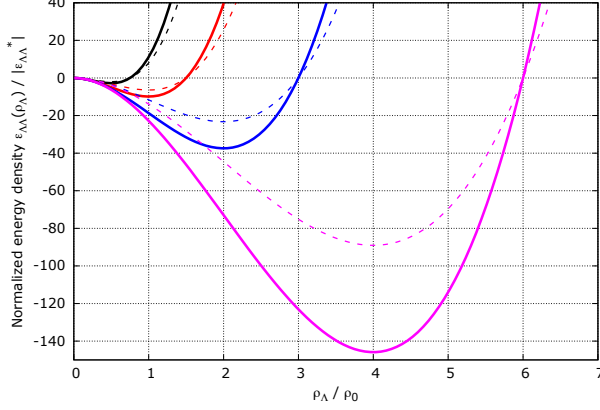


FIG. 4. (Color online) Normalized energy density  $\epsilon_{\Lambda\Lambda}(\rho_\Lambda)/|\epsilon_{\Lambda\Lambda}^*|$  for the same parameters as in Fig. 3.

The potential and energy density behavior, displayed in Figs.3 and 4, show that this choice of parameters spans a wide range of qualitative behaviors of the energy functional.

### C. Application of the energy-density functionals to hypernuclei

For the sake of completeness, we recall here the results obtained in [12, 13], also used in the present work, describing the implementation of the Hartree-Fock approach in the hypernuclear case. Nucleons and lambdas in the medium acquire an effective mass which is generated by the momentum dependence of the interaction. The description of finite nuclei requires to disentangle the momentum dependent part of the in-medium potential (the correction to the masses) from the momentum independent one, hereafter called the local part. The local energy density is defined by:

$$\frac{\hbar^2}{2m_N}\tau_N + \epsilon_{NN}(\rho_N) = \frac{\hbar^2}{2m_N^*}(\rho_N)\tau_N + \epsilon_{NN}^{loc}(\rho_N), \quad (29)$$

$$\frac{\hbar^2}{2m_\Lambda}\tau_\Lambda + \epsilon_{N\Lambda}(\rho_N, \rho_\Lambda) = \frac{\hbar^2}{2m_\Lambda^*}(\rho_N)\tau_\Lambda + \epsilon_{N\Lambda}^{loc}(\rho_N, \rho_\Lambda), \quad (30)$$

which can be recasted as:

$$\epsilon_{NN}^{loc} = \epsilon_{NN} - \frac{3\rho_N\hbar^2}{10} \left(\frac{6\pi^2\rho_N}{g_N}\right)^{2/3} \left(\frac{1}{m_N^*} - \frac{1}{m_N}\right) \quad (31)$$

$$\epsilon_{N\Lambda}^{loc} = \epsilon_{N\Lambda} - \frac{3\rho_\Lambda\hbar^2}{10} \left(\frac{6\pi^2\rho_\Lambda}{g_\Lambda}\right)^{2/3} \left(\frac{1}{m_\Lambda^*} - \frac{1}{m_\Lambda}\right) \quad (32)$$

where  $\epsilon_{NN}$  is derived from the Skyrme functional [28, 29] and  $\epsilon_{N\Lambda}$  is given by Eq. (4). We have already seen that the nucleon contribution to the lambda potential,  $\epsilon_{N\Lambda}$ , is much bigger than the  $\Lambda$  contribution,  $\epsilon_{\Lambda\Lambda}$ . For this reason, the contribution of

TABLE II. Parameters of the  $\Lambda$ -effective mass given by Eq. (34) for the functionals considered in this paper.

Force	$\mu_1$	$\mu_2$	$\mu_3$	$\mu_4$
DF-NSC89 [12, 13]	1	1.83	5.33	6.07
DF-NSC97a [13]	0.98	1.72	3.18	0
DF-NSC97f [13]	0.93	2.19	3.89	0

the  $\Lambda\Lambda$  interaction to the  $\Lambda$  effective mass can be considered as a small corrections, and it has been neglected in Ref. [13]. We can therefore write:

$$\epsilon_{\Lambda\Lambda}^{loc}(\rho_\Lambda) = \epsilon_{\Lambda\Lambda}(\rho_\Lambda). \quad (33)$$

In Eqs. (31) and (32) the local part of the energy density requires the knowledge of the effective masses  $m_N^*$  and  $m_\Lambda^*$ . The nucleon effective mass  $m_N^*$  is given from the Skyrme interaction [28, 29]. The effective mass of the  $\Lambda$  particles is mainly generated by the momentum dependence of the  $N\Lambda$  interaction, and it can be deduced from the BHF calculations. The result is expressed as a polynomial in the nucleonic density  $\rho_N$  as [12],

$$\frac{m_\Lambda^*(\rho_N)}{m_\Lambda} = \mu_1 - \mu_2\rho_N + \mu_3\rho_N^2 - \mu_4\rho_N^3. \quad (34)$$

The values for the parameters  $\mu_{1-4}$  for the functional considered here are given in Table II and the density dependence of the effective mass is shown in Fig. 5. Since the effective mass is only necessary in the description of finite nuclei, we have limited the densities to values around saturation densities in Fig. 5. We can again observe, on the left panel, that the three functionals show a qualitatively similar behavior for the  $\Lambda$  effective mass at low density, with the stiffest model DF-NSC97f showing as expected the strongest momentum dependence.

Given the functional form of  $\epsilon^{loc}$  and  $m^*$  for the nucleons and the lambdas, Eq. (3) can be rewritten in a form which explicitly disentangle the terms coming from the local operator  $\hat{\rho}$  and the non-local operator  $\hat{\tau} = \vec{\nabla}\hat{\rho}\vec{\nabla}$  as,

$$\epsilon(\rho_N, \rho_\Lambda, \tau_N, \tau_\Lambda) = \frac{\hbar^2}{2m_N^*(\rho_N)}\tau_N + \frac{\hbar^2}{2m_\Lambda^*(\rho_N)}\tau_\Lambda + \epsilon_{NN}^{loc}(\rho_N) + \epsilon_{N\Lambda}^{loc}(\rho_N, \rho_\Lambda) + \epsilon_{\Lambda\Lambda}(\rho_\Lambda). \quad (35)$$

Minimizing the total energy, defined from the density functional (35), and using the Skyrme model for the nucleonic part, we obtain the usual Schrödinger equation ( $i = N, \Lambda$ ),

$$\left[ -\nabla \cdot \frac{\hbar^2}{2m_i^*(r)}\nabla + V_i(r) - iW_i(r)(\nabla \times \sigma) \right] \phi_{i,\alpha}(r) = -e_{i,\alpha}\phi_{i,\alpha}(r), \quad (36)$$

where the nucleon potential  $V_N$  is defined as,

$$V_N(r) = v_N^{unif}(r) + \frac{\partial}{\partial\rho_N} \left( \frac{m_\Lambda}{m_\Lambda^*(\rho_N)} \right) \times \left( \frac{\tau_\Lambda}{2m_\Lambda} - \frac{3}{5} \frac{(3\pi^2)^{2/3}\hbar^2}{2m_\Lambda} \rho_\Lambda^{5/3} \right), \quad (37)$$



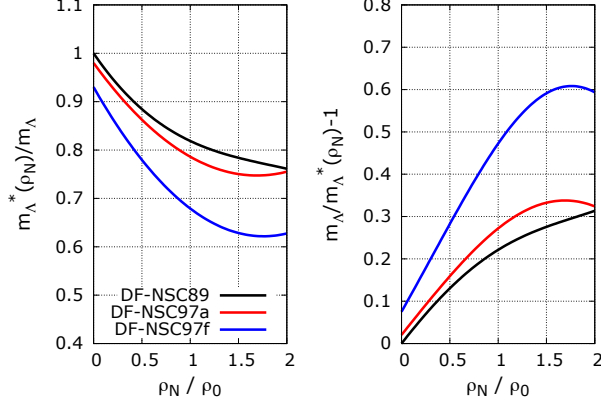


FIG. 5. (Color online) Ratio of the effective and bare  $\Lambda$  mass  $m_{\Lambda}^*(\rho_N)/m_{\Lambda}$  (left) and  $1 - m_{\Lambda}^*/m_{\Lambda}$  (right) as a function of the nucleon density  $\rho_N$  (in units of the saturation density  $\rho_0$ ) for the functionals DF-NSC89, DF-NSC97a and DF-NSC97f.

The hyperon potential  $V_{\Lambda}$  is given by,

$$V_{\Lambda}(r) = v_{\Lambda}^{unif} - \left( \frac{m_{\Lambda}}{m_{\Lambda}^*(\rho_N)} - 1 \right) \frac{(3\pi^2)^{2/3} \hbar^2}{2m_{\Lambda}} \rho_{\Lambda}^{2/3}. \quad (38)$$

As in the uniform case, the hyperon potential  $V_{\Lambda}$  is decomposed into two terms,  $V_{\Lambda} = V_{\Lambda}^{(N)} + V_{\Lambda}^{(\Lambda)}$  where,

$$V_{\Lambda}^{(N)}(r) = v_{\Lambda}^{(N),unif} - \left( \frac{m_{\Lambda}}{m_{\Lambda}^*(\rho_N)} - 1 \right) \frac{(3\pi^2)^{2/3} \hbar^2}{2m_{\Lambda}} \rho_{\Lambda}^{2/3} \quad (39)$$

$$V_{\Lambda}^{(\Lambda)}(r) = v_{\Lambda}^{(\Lambda),unif}. \quad (40)$$

The factor  $(m_{\Lambda}/m_{\Lambda}^*(\rho_N) - 1)$  in Eq. (39) is displayed on the right panel of Fig. 5, showing that it is quite large around saturation density, between 0.2 and 0.5. The modification of the lambda potential in nuclei with respect to the uniform potential can be quite important as scales approximately with the kinetic energy density of the lambdas.

### III. DETERMINATION OF THE $\Lambda\Lambda$ FUNCTIONAL

In the following we will use the previous formalism to perform calculations in finite nuclei, and to determine the parameters of the  $\Lambda\Lambda$  functional. In the case of single- $\Lambda$  hypernuclei there is no  $\Lambda\Lambda$  interaction, and the corresponding terms in the functional shall therefore not be considered. We therefore set  $\varepsilon_{\Lambda\Lambda} = 0$  for single- $\Lambda$  hypernuclei, while for double and many- $\Lambda$  hypernuclei, we consider the original expression (5) for  $\varepsilon_{\Lambda\Lambda}$ .

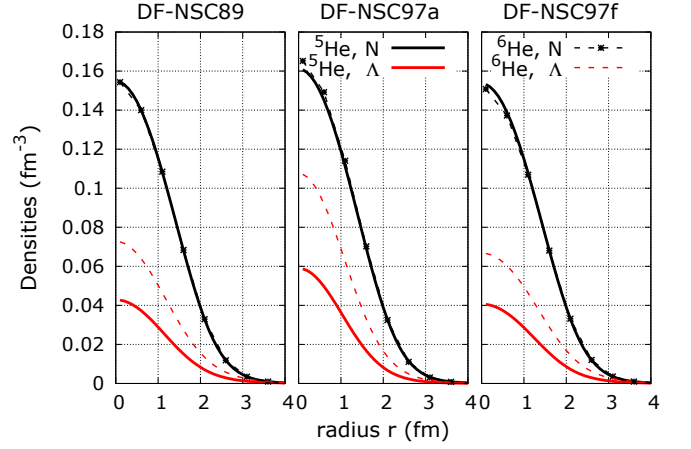


FIG. 6. (Color online) Density profiles in  ${}^4\text{He}$  isotopes with the addition of one or two  $\Lambda$  hyperons. Black (red) lines: nucleon ( $\Lambda$ ) density. Full (dashed) lines: one (two)  $\Lambda$  is added to the  ${}^4\text{He}$  nucleus. Three different functionals, from left to right DF-NSC89, DF-NSC97a, and DF-NSC97f are considered.

#### A. The average $\Lambda$ -density in hypernuclei

According to Eq. (17), the bond energy and the average density in the double- $\Lambda$  hyper nucleus  ${}^A_{\Lambda\Lambda}Z$  are closely related. The bond energy can be experimentally constrained, but no experimental determination of the average  $\Lambda$ -density exists yet. Fig. 6 displays the nucleon and  $\Lambda$  densities in  ${}^5_{\Lambda}\text{He}$  and  ${}^6_{\Lambda\Lambda}\text{He}$  for the functionals DF-NSC89, DF-NSC97a and DF-NSC97f, using SLy5 for the nucleons. The average single and double- $\Lambda$ -densities (Fig. 6) show a moderate dependence on the model.

A definition of the average  $\Lambda$ -density from the  $\Lambda$ -density profile is required in order to properly define the parameter  $x_{\Lambda}(A)$ . Fig. 6 clearly shows that the  $\Lambda$ -density profile does not have a flat behavior at the center of a small hypernuclear system; as a consequence, the standard deviation from the average will be quite large. Table III displays the calculated average double- $\Lambda$  densities and standard deviations for the same functionals as in Fig. 6, using three different ways to estimate the average  $\Lambda$ -density:

$$\langle \rho_{\Lambda} \rangle_{\Lambda} = \frac{\int d^3r \rho_{\Lambda} \rho_{\Lambda}}{\int d^3r \rho_{\Lambda}} \quad (41)$$

$$\langle \rho_{\Lambda} \rangle_N = \frac{\int d^3r \rho_{\Lambda} \rho_N}{\int d^3r \rho_N} \quad (42)$$

$$\langle \rho_{\Lambda} \rangle_T = \frac{\int d^3r \rho_{\Lambda} \rho_T}{\int d^3r \rho_T} \quad (43)$$

where  $\rho_T = \rho_N + \rho_{\Lambda}$ . The standard deviation is defined as  $\sigma_i = \sqrt{\langle \rho_{\Lambda}^2 \rangle_i - \langle \rho_{\Lambda} \rangle_i^2}$ , with  $i = \Lambda, N$  or  $T$ . The comparison between the different ways to extract the average  $\Lambda$ -density in Table III shows a 15% deviation. As anticipated, the standard deviation is very large, almost of the order of the average

TABLE III. Calculations of average  $\Lambda$ -densities in  ${}^6_{\Lambda\Lambda}\text{He}$  (in  $\text{fm}^{-3}$ ) for the functionals DF-NSC89, DF-NSC97a and DF-NSC97f.

	DF-NSC89	DF-NSC97a	DF-NSC97f
$10^2 \langle \rho_\Lambda \rangle_\Lambda$	2.25	3.69	2.31
$10^2 \langle \rho_\Lambda \rangle_N$	2.64	3.48	2.65
$10^2 \langle \rho_\Lambda \rangle_T$	2.51	3.55	2.53
$10^2 \sigma_\Lambda$	1.97	2.89	1.85
$10^2 \sigma_N$	1.85	2.74	1.76
$10^2 \sigma_T$	1.90	2.79	1.80

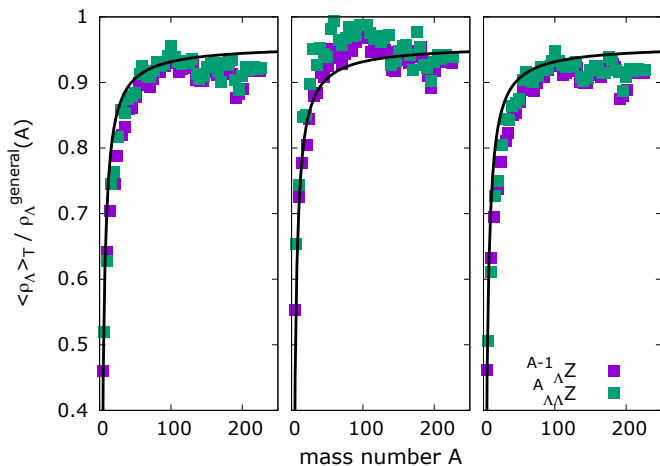


FIG. 7. (Color online) Ratios of the  $\Lambda$  density (eq.(43)) over the approximate relation (eq.(44)) as a function of baryon number for  $\Lambda = 1$  (red) and  $\Lambda = 2$  (green). A fit is also shown.

value. It is therefore difficult to properly define an average  $\Lambda$ -density in  ${}^6_{\Lambda\Lambda}\text{He}$ .

A general expression for the average  $\Lambda$ -density in hypernuclei was given in Ref. [13], supposing that the  $\Lambda$ -density scales with the nucleon density. The following general expression [13] was therefore proposed:

$$\rho_\Lambda^{\text{general}}(A) \approx \Lambda \frac{\rho_0}{A}, \quad (44)$$

where  $\Lambda=1$  for single- $\Lambda$  hypernuclei and  $\Lambda=2$  for double- $\Lambda$  hypernuclei. Fig. 7 shows the ratio of the microscopically calculated average  $\Lambda$ -density  $\langle \rho_\Lambda \rangle_T$ , over the general expression (44). The general expression is rather well satisfied for large  $A$ , but a systematic deviation is observed for small  $A$ . The fit of the deviation is also shown in Fig. 7 and we obtain,

$$\langle \rho_\Lambda \rangle_T \approx \rho_\Lambda^{\text{general}}(A) \left[ 0.957 - 2.54A^{-1} \right]. \quad (45)$$

This shows that Eq. (44) of Ref. [13] is not valid for  $A \lesssim 50$ . It should be noted that we have used the expression  $\langle \rho_\Lambda \rangle_T$ , see Eq. (43), as a reference to estimate the average  $\Lambda$ -density. Similar results are obtained with  $\langle \rho_\Lambda \rangle_N$  for large nuclei, but the definition  $\langle \rho_\Lambda \rangle_\Lambda$  gives a systematic increase by a factor of about 2 compared to the two other definitions, in large nuclei.

## B. Empirical determination of the term $\tilde{\epsilon}_{\Lambda\Lambda}$

The relation between the  $\Delta B_{\Lambda\Lambda}(A)$  parameters and  $x_\Lambda(A)$  is given by Eq. (17) for a given hypernucleus  $A$ . However, while the bond energy can be determined from experimental mass measurements, the average  $\Lambda$ -density have never been measured. We have seen in the previous section that the average  $\Lambda$ -density depends on the functional and that the standard deviation in  ${}^6_{\Lambda\Lambda}\text{He}$ , the nucleus for which the best measurement of the bond energy exists [34, 35], is almost comparable with the average  $\Lambda$ -density. Two different methods are used to set the value of  $x_\Lambda$ :

EmpA: The value of  $x_\Lambda({}^6_{\Lambda\Lambda}\text{He})$  is fixed to an average value ( $=1/6$ ) in  ${}^6_{\Lambda\Lambda}\text{He}$ , independently of the functional.

EmpB: The value of  $x_\Lambda$  is optimized to obtain a fixed bond energy ( $\approx 1$  MeV, consistent with Refs. [34, 35] or  $\approx 5$  MeV, as suggested in Ref. [33]) in He for each functional.

In prescription EmpA, the relation between the bond energy and the functional is based on the local density approximation (see Eq. (17) and App. A for more details). It is therefore interesting to calculate the bond energy which is obtained from the microscopic HF calculations, in order to estimate the accuracy of the local density approximation. Doing so for DF-NSC89, DF-NSC97a and DF-NSC97f, and varying the parameter  $x$  from 1/2 to 4, the difference between the bond energy set to determine the parameters and the one calculated from HF calculation in  ${}^6_{\Lambda\Lambda}\text{He}$  is less than 20%. A larger difference is found between the parameter  $x_\Lambda = 1/6$  and the average  $\Lambda$ -density in  ${}^6_{\Lambda\Lambda}\text{He}$ . We conclude that the prescription EmpA, based on the local density approximation, cannot provide accurate parameters. This is related to the analysis of the  $\Lambda$ -density profile in  ${}^6_{\Lambda\Lambda}\text{He}$  which is not flat enough to allow for the local density approximation (see Tab. III).

In the present approach, given by the prescription EmpB, the value of  $x_\Lambda$  is not fixed a priori but it is varied and correlated with the bond energy determined from the HF calculation. In such a way, the parameter  $x_\Lambda$  is treated as a variational parameter allowing to fit the bond energy in He. The correlation between the parameter  $x_\Lambda$  and the bond energy  $\Delta B_{\Lambda\Lambda}(A=6)^{\text{HF}}$  is shown in Fig. 8, for the functional DF-NSC89 with  $x = 1/2$  and DF-NSC89 with  $x = 4$ . The results for the functionals DF-NSC89, DF-NSC97a and DF-NSC97f using this empirical prescription (called EmpB hereafter) are given in Tab. IV, obtained from the adjustment to the bond energy. Since a large arbitrariness is associated to the  $\Lambda\Lambda$  functional, the simplest polynomial form that allows for the needed repulsion at high density, and corresponds to a bond energy of 1 MeV in  ${}^6\text{He}$  and neighboring hypernuclei is chosen. We will therefore use the functionals of Table IV for the calculations of this work. Allowing for this large variation of the  $x$  parameter, the largely unknown behavior at supersaturation is therefore decoupled from the behavior at the very low densities implied for the hypernuclei.

Finally, Fig. 9 compares the potentials  $v_\Lambda^{(\Lambda),unif}$  obtained from the functionals DF-NSC89, DF-NSC97a and DF-



TABLE IV. Prescription EmpB. We present the adjustment of the parameter  $x_\Lambda(4)$  to the bond energy ( $\approx 1$  or 5 MeV in  ${}^4\text{He}$ ), the values of the parameters  $\tilde{\alpha}_7^B$  and  $\tilde{\alpha}_8^B$ , and the ratio of the  $\Lambda$ -density to the saturation density in He.

Pot. $\Lambda\text{N}$	DF-NSC89	DF-NSC89	DF-NSC97a	DF-NSC97a	DF-NSC97f	DF-NSC97f
Pot. $\Lambda\Lambda$	EmpB1	EmpB2	EmpB1	EmpB2	EmpB1	EmpB2
$x$	1/2	4	1/2	4	1/2	4
$\Delta B_{\Lambda\Lambda}(A=6) = 5 \text{ MeV}$						
$\tilde{\alpha}_7$	150	80.82	150	70.64	160.48	100.33
$\tilde{\alpha}_8$	1250	84.19	1250	73.59	1337	104.51
$\Delta B_{\Lambda\Lambda}(6)^{HF}$	5.05	4.86	5.17	5.03	4.84	5.00
$x_\Lambda$	0.125	0.2	0.125	0.23	0.115	0.16
$\Delta B_{\Lambda\Lambda}(A=6) = 1 \text{ MeV}$						
$\tilde{\alpha}_7$	36.05	25.53	39.46	22.85	49.24	35.25
$\tilde{\alpha}_8$	300.48	26.60	328.81	23.81	410.32	36.72
$\Delta B_{\Lambda\Lambda}(6)^{HF}$	0.97	1.1	0.95	1.04	0.98	1.05
$x_\Lambda$	0.1	0.125	0.09	0.14	0.07	0.09

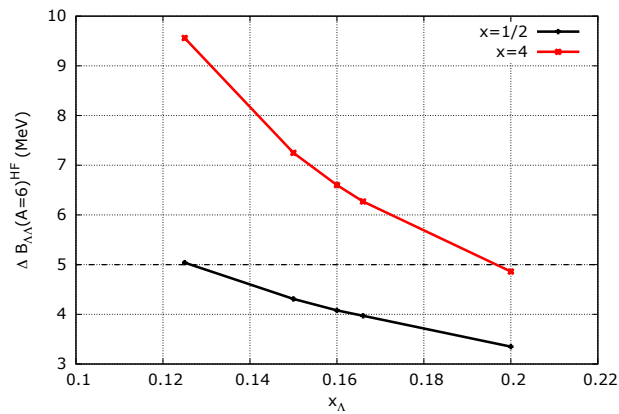


FIG. 8. (Color online) Relation between the parameter  $x_\Lambda({}^6\text{He})$  and the bond energy set to 5 MeV (16) for He extracted from the HF calculation with the functional DF-NSC89 with  $x = 1/2$  and DF-NSC89 with  $x = 4$ .

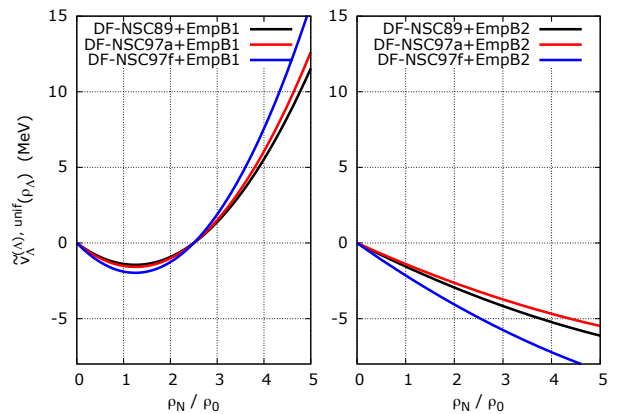


FIG. 9. (Color online) Comparison of the potential  $v_{\Lambda}^{(\Lambda),unif}(\rho_N, \rho_\Lambda)$  obtained with the prescription EmpB1 and EmpB2 (see legend) as a function of the nucleon density  $\rho_N$  (in units of the saturation density  $\rho_0$ ) for the functionals DF-NSC89, DF-NSC97a and DF-NSC97f. We have fixed  $\Delta B_{\Lambda\Lambda} = 1$  MeV and the fraction of  $\Lambda$  to be 20%. On the left panel, we have fixed  $x = 1/2$ , while on the right,  $x = 4$ .

NSC97f associated to the empirical prescriptions EmpB1 and EmpB2, where the bond energy is fixed to 1 MeV. Around saturation density, the different models shown in Fig. 9 predict negative values ranging from -1 to -2 MeV. At densities higher than normal nuclear saturation density, the prescription EmpB1 makes the potential  $v_{\Lambda}^{(\Lambda),unif}$  much stiffer than the prescription EmpB2. It is also interesting to compare the empirical models shown in Fig. 9 with the initial ones displayed on Fig. 2: the empirical prescription EmpB1 produces the stiffest potential while EmpB2 the softest. Our empirical prescription increases the exploratory domain of variation for the  $\Lambda\Lambda$  potential, as well as includes the initial potential.

### C. Calculations in hypernuclei

In the following, we consider the three functionals DF-NSC89, DF-NSC97a and DF-NSC97f corrected with the empirical prescriptions EmpB1 and EmpB2 associated to a bond energy of 1 MeV. We therefore consider 6  $\text{N}\Lambda + \Lambda\Lambda$  functionals, corresponding to Table IV, together with SLy5 [23] for the NN functional. For each  $\text{N}\Lambda$  functional (DF-NSC89, DF-NSC97a and DF-NSC97f) the first one (e.g. DF-NSC89-EmpB1) corresponds to the lowest hyperon density in nuclear

matter ( $x=1/2$ ), whereas the second one (e.g. DF-NSC89-EmpB2) corresponds to the largest hyperon density ( $x=4$ ).

It should be noted that the present work is focused on the uncertainty generated by the  $\Lambda$  related functionals on the number of bound systems. The uncertainties generated by the NN functional itself have already been studied on the nuclear chart and is typically of 7% on the number of bound nuclei [19].

In the present work, the hypernuclear charts are calculated for even-even-even hypernuclei. Since spherical symmetry is imposed, only magic lambda number hypernuclei are considered. As mentioned above, the spin-orbit interaction is known to be weak in the  $\Lambda$  channel [22], a factor 100 lower than in the nucleonic sector [36], according to experimental data. The  $\Lambda$  magic numbers are therefore expected to be close to the harmonic oscillator ones: 2, 8, 20, 40, and 70. Calculations are performed for hypernuclear charts corresponding to these specific numbers of  $\Lambda$ .

#### IV. THE HYPERDRIPLINES

The  $\Lambda$  dripline has been studied in Ref. [12] with a similar HF approach, showing that the maximum number of bound  $\Lambda$  in an hypernucleus is about 1/3 of the number of nucleons. We aim here to provide a more general study of hyperdriplines, namely also showing the evolution of the proton and neutron driplines with the number of hyperons.

Figure 10 displays the microscopically calculated hypernuclear charts for  $\Lambda=0, 2, 8, 20, 40$  and  $70$  using the DF-NSC89+EmpB1 functional. Adding  $\Lambda$ 's to a nucleus increases the binding energy for  $\Lambda < 40$ , but conversely decreases it for  $\Lambda=40$  and  $70$ . This is due to the balance between the attractive  $\Lambda N$  and  $\Lambda\Lambda$  functionals and the progressive energy filling of the  $\Lambda$  states in the mean  $\Lambda$  potential. Fig. 10 also shows that with a large number of lambdas, the corresponding hypernuclear chart is shifted towards larger  $N, Z$  values. This effect is mainly due to the  $\Lambda N$  functional and is related to the maximum fraction of 1/3 of hyperons with respect to nucleons, as mentioned above.

To get a more accurate estimation of the dripline, Fig. 11 displays the dripline neutron numbers for each  $Z$  value in the case of  $\Lambda=20$  and for the 6 ( $\Lambda\Lambda+\Lambda N$ ) functionals that we consider. The dripline is here defined when the chemical potential becomes positive. The results are rather similar among the various functionals. This shows that despite the very large differences among these functionals both in the  $N\Lambda$  and  $\Lambda\Lambda$  channels, the error bars are not so large for the drip-line determination, contrarily to what could be expected. This may be due to the narrower density range corresponding to finite hyper-nuclei compared to hyper-nuclear matter, since the 6 functionals provide similar potentials for subsaturation densities.

The number of bound even-even-even hypernuclei found for  $\Lambda \leq 70$  and  $Z \leq 120$  are given in Table V. The dispersion due to the uncertainty on the  $\Lambda$ -related functional is rather small: the average total number of even-even-even hypernuclei for  $\Lambda=0, 2, 8, 20, 40,$  and  $70$  is  $9770 \pm 429$ . Interpolating the number of even-even-even hypernuclei on the whole hy-

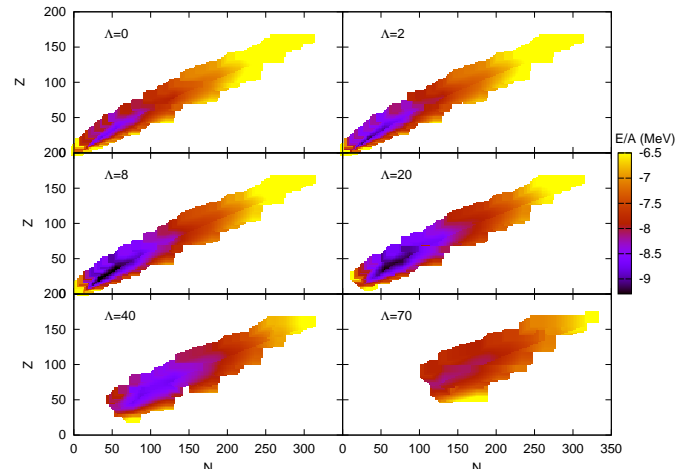


FIG. 10. (Color online) Hypernuclear charts for magic  $\Lambda$  numbers calculated with the DF-NSC89+EmpB1 functional

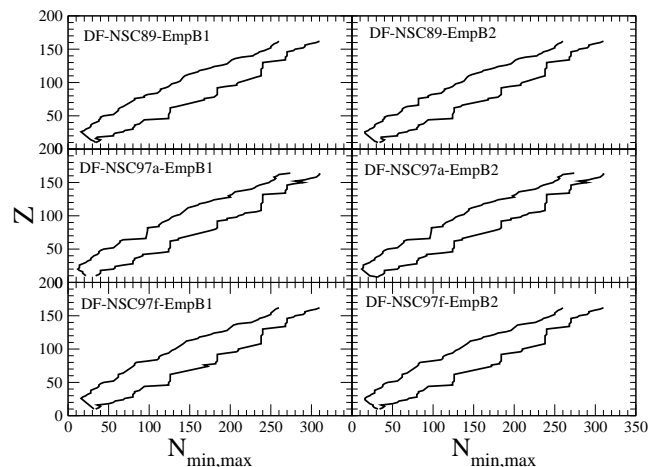


FIG. 11. (Color online) Minimal (upper line) and maximal (lower line) neutron number value for hyper nuclei with  $\Lambda=20$  using the 6 functionals described in Table IV

pernuclear chart, provides  $59538 \pm 4020$  hypernuclei with a larger relative systematic uncertainties, which can be inferred from the interpolation procedure. The interpolation is linearly performed between the calculated magic  $\Lambda$  hypercharts.

The corresponding uncertainty is calculated from the dispersion of the total number of even-even-even hypernuclei obtained with the six ( $\Lambda\Lambda+\Lambda N$ ) functionals. It should also be noted that magic nuclei are specific nuclei in the hypernuclear channel and therefore the interpolation procedure is not optimal. Considering the uncertainty on the bond energy (between

1 MeV and 5 MeV as explained in the previous section), the number of estimated even-even-even nuclei is  $61460 \pm 4300$ . The total number of hypernuclei, considering the odd ones is therefore  $491680 \pm 34400$ . If the uncertainty of the NN functional [19] is included (here in a decorrelated way), the total number of hypernuclei with  $\Lambda \leq 70$  and  $Z \leq 120$  is  $491680 \pm 59000$ .

The relative uncertainty is therefore of about 4% on the magic  $\Lambda$  hypernuclear charts. It is determined using the mean value and the corresponding standard deviation considering the 6 ( $\Lambda N + \Lambda\Lambda$ ) functionals. It should be noted that the DF-NSC97a functional is more attractive than the other functionals, which is the main contribution to the uncertainties on the number of bound hypernuclei. If the bond energy requirement is changed from 1 MeV to 5 MeV, the variation among the 6 newly derived functionals is about 5%. All in all, it is safe to consider an upper limit of 7% uncertainty due to the  $\Lambda\Lambda$  and the  $\Lambda N$  functionals on the magic  $\Lambda$  hypernuclear charts. In the case of interpolated values, the uncertainty is of about 7% considering the 6 ( $\Lambda N + \Lambda\Lambda$ ) functionals, plus 5% from changing the bond energy requirement from 1 MeV to 5 MeV. These values should be compared to the relative uncertainty of about 7% when the NN Skyrme functional is changed [19] on the nuclear chart. It shows that the uncertainty from the  $\Lambda$ -related functionals is not significantly larger than the one from the NN functional. This is due to the focused range of densities (i.e. below the saturation one) relevant for hypernuclei, as mentioned above.

## V. HYPERNUCLEAR STRUCTURE

### A. Binding energy: fusion and fission of hypernuclei

It may be relevant to study how the presence of hyperons impacts the most bound hypernuclei per baryon, which is known to be in the Fe-Ni region in the case of nuclei.

Fig. 12 displays the evolution of the largest  $B/A$  value as a function of the number of hyperons in hypernuclei calculated with 4 ( $\Lambda N + \Lambda\Lambda$ ) functionals. A remarkable agreement between the four functionals considered is observed, which may suggest that the theoretical uncertainty on the problem of hypernuclear binding is relatively under control, at least in the low density region corresponding to nuclei. It would be very interesting to know if this agreement is kept using relativistic functionals as in Ref. [2]. In the case of DF-NSC89+EmpB1 and for  $\Lambda=2$  or 8, the optimal  $Z$  value is not much changed compared to the Nickel-Iron area. For a number of hyperons from 20 and larger the most bound hypernucleus is obtained for larger  $Z$ , typically for Zr, Ce and Pb. The results are qualitatively similar with the other functionals, except in the case of DF-NSC97a+EmpB1 and DF-NSC97f+EmpB1, for  $2\Lambda$  hypernuclei: the addition of only  $2\Lambda$  makes Si and, respectively, Ti the most bound nucleus in terms of binding energy per baryon. This result shows the non-negligible impact of hyperons on the binding energy of the system.

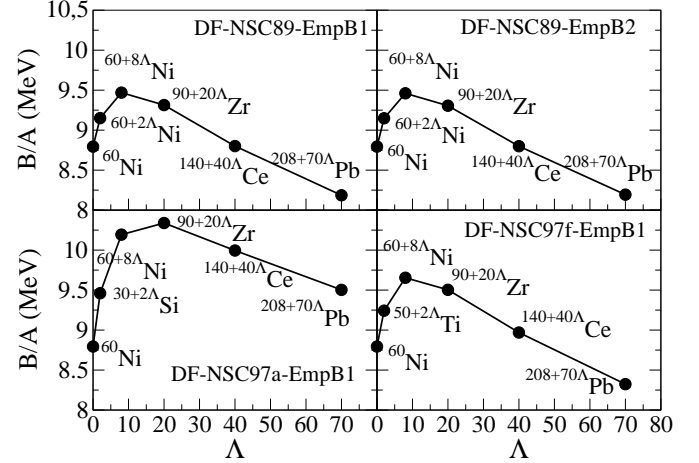


FIG. 12. (Color online) Hypernuclei with maximum binding energy per baryon as a function of  $\Lambda$  for the DF-NSC89+EmpB1, DF-NSC89+EmpB2, DF-NSC97a+EmpB1, DF-NSC97f+EmpB1 functionals

### B. Magicity

Several signals of the evolution of the magic gaps along the nuclear chart have been obtained these last decades [37]. It may therefore be relevant to extend prediction of magicity to the hypernuclear chart. The two protons or two neutrons gap are known to be a relevant quantity in order to provide a first insight on magicity features in nuclei.

It is known that shell effects can vanish in the case of very neutron rich nuclei [38, 39] because of the smoothness of the neutron skin triggering a weakening of the spin-orbit effect, and therefore its corresponding magic numbers. This is the case for hypernuclei with a low number of  $\Lambda$ . But in the case of  $\Lambda=40$ , Figure 13 shows a restoration of the  $Z=28$  magicity for the very neutron-rich hypernickels with  $70 < N < 80$ : the spin-orbit weakening of the  $Z=28$  magic number for very neutron-rich hypernuclei is reduced by the presence of hyperons. A similar effect is observed for  $\Lambda=70$  and the  $N=186$  magic number: it is restored for  $82 < Z < 98$ . The present results were obtained with DF-NSC89+EmpB1 and similar results are obtained with the other functionals. A weakening of the  $N=28$  shell closure is found for  $\Lambda < 8$  in agreement with the previous results. Also a  $Z=40$  weakening is observed for these hypernuclei.

Fig. 14 displays the neutron, proton and hyperon densities for the triply magic hypernucleus  $^{208+\Lambda}\text{Pb}$  with  $\Lambda=2, 8, 20, 40$ , and 70. The proton and neutron densities are almost not impacted by the hyperons addition, showing a relative independence of the hyperons with respect to the nucleonic core. The results are in agreement with Ref. [12] where the Skyrme parameterisation SIII was used and the  $\Lambda\Lambda$  functional neglected. This validates the present approach and more globally the mi-

TABLE V. Number of bound even-even-even hypernuclei for  $\Lambda < 70$  and  $Z < 120$ 

Number of nuclei	DF-NSC89	DF-NSC89	DF-NSC97a	DF-NSC97a	DF-NSC97f	DF-NSC97a
	+EmpB1	+EmpB2	+EmpB1	+EmpB2	+EmpB1	+EmpB2
$\Lambda=0$	1578	1578	1573	1573	1578	1578
$\Lambda=2$	1628	1640	1617	1619	1634	1621
$\Lambda=8$	1647	1644	1692	1680	1750	1749
$\Lambda=20$	1650	1681	1696	1724	1675	1683
$\Lambda=40$	1713	1736	1961	1972	1722	1716
$\Lambda=70$	1162	1237	1746	1886	1127	1152
Total	9378	9516	10285	10454	9486	9499
Total interpolated	56140	57287	64459	65587	56646	56809

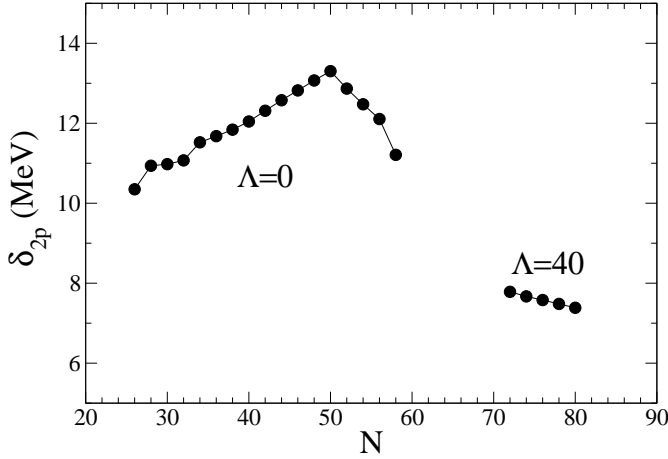


FIG. 13. (Color online) The 2 protons gap in the bound Nickel isotopes for  $\Lambda=0$  and  $\Lambda=40$ , defined as  $\delta_{2p} \equiv S_{2p}(A, Z) - S_{2p}(A+2, Z+2)$ , calculated with the DF-NSC89+EmpB1 functional

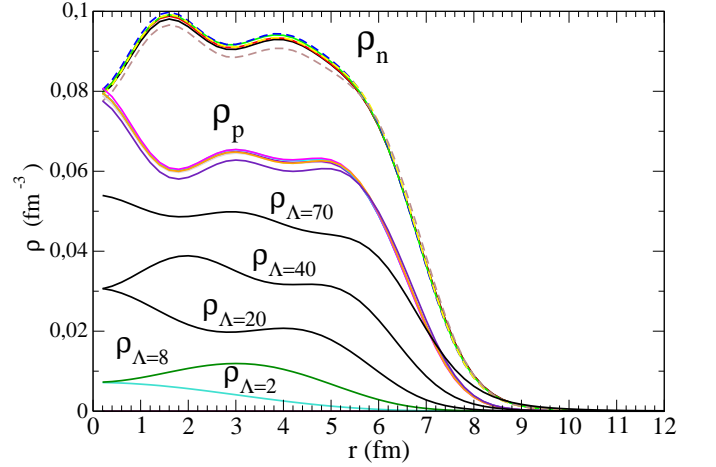


FIG. 14. (Color online) Baryonic densities for the triply magic  $^{208+\Lambda}\text{Pb}$  hypernucleus with  $\Lambda=2, 8, 20, 40, 70$

crossopic prediction of hypernuclei properties.

### C. Bubbles and haloes

Bubbles and haloes effects have recently been studied in hypernuclei [2]. Hyperons are more diffuse in a nucleus than nucleons. This could be due to the weaker  $\Lambda\Lambda$  attraction compared to the NN one, generating an hyperon saturation density about 1/3 smaller than the nucleonic one. This may also be due to the  $\Lambda\Lambda$  functional which is much more intense in Ref. [2] compared to the one used in the present work. It emphasizes the importance of taking into account the bond energy in order to constrain the  $\Lambda\Lambda$  functional, as depicted in section II and III.

It is well known that the addition of a single hyperon shrinks the nuclear core [40], both from predictions and from

measurements. It is therefore relevant to study the effect on the neutron and proton densities of a large number of hyperons. We find no large effect of the increase of the  $\Lambda$  number on the proton nor on the neutron density in  $^{16}\text{O}$ . In the case of  $^{104+40\Lambda}\text{Cr}$ , the lambdas act like a glue between protons and neutrons and even drive the proton to larger radii, as shown by Fig. 15. A similar effect is observed on the neutron density. This is due to the fact that hyperons attract nucleons at larger radii. It should also be noted that the halo effect in  $^{104+40\Lambda}\text{Cr}$  is rather small compared to predictions using RMF approaches [2].

In the case of bubbles [2, 41, 42], there is no strong impact of the increase of number of hyperons on the depletion. Figure 16 displays the proton, neutrons and hyperons densities in  $^{34}\text{Si}$  with no hyperons, and the addition of 2 and 8 hyperons. As described above, the proton and neutron densities are almost not impacted by the addition of hyperons and therefore the predicted proton depletion in  $^{34}\text{Si}$  remains. This small in-

## VI. CONCLUSIONS

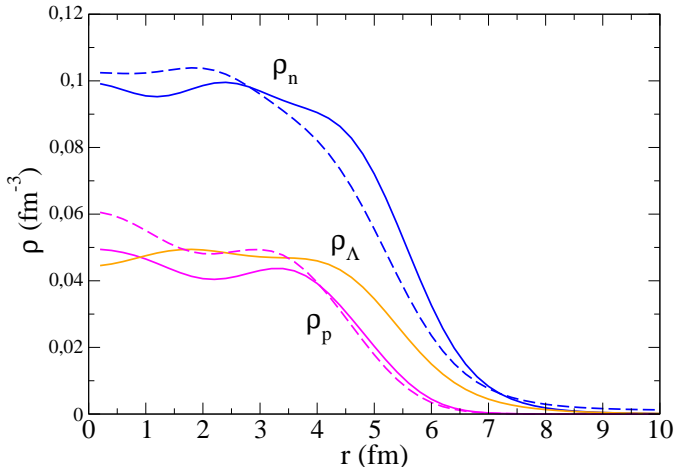


FIG. 15. (Color online) Baryons densities for the magic  $^{144}\text{Cr}_{40\Lambda}$  hypernucleus (solid lines). The neutron and proton densities for the  $^{104}\text{Cr}$  nucleus are in dashed lines.

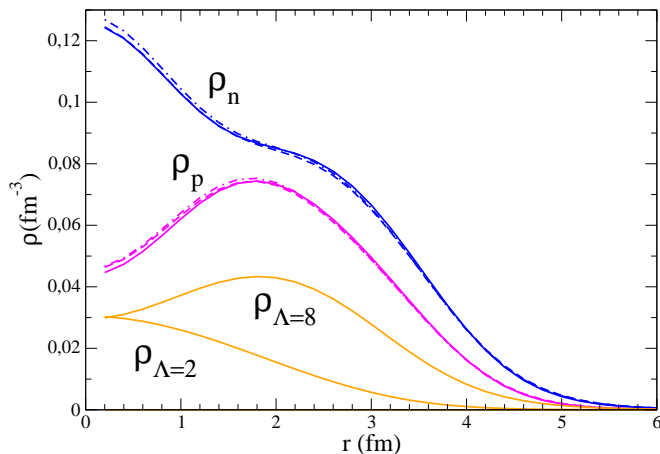


FIG. 16. (Color online) Baryons densities for  $^{34+\Lambda}\text{Si}$  hypernucleus with  $\Lambda=2$  (dot-dashed lines for neutron and proton densities) and  $\Lambda=8$  (solid lines). The neutron and proton densities for the  $^{34}\text{Si}$  nucleus are in dashed lines.

terdependence is at variance with relativistic calculations obtained with the RMF approach [2].

In summary the present results show that the effect of hyperons on the nucleon core is much weaker than in the RMF case. This may be due to the different  $(\text{N}\Lambda+\Lambda\Lambda)$  functionals that are used in the two approaches. It should be noted that the present  $(\text{N}\Lambda+\Lambda\Lambda)$  functionals are constrained with bond energy requirements.

In this work, we have proceeded in two steps: first we have discussed the properties of the functionals, based on BHF data, and proposed an empirical prescription for the  $\Lambda\Lambda$  term. Then, we have explored the hypernuclear chart allowing the functional to vary inside our domain of uncertainty.

In the first step of the paper, we found that the low density part of the functional is well determined by the value of the bond energy, while the high density part is determined by the unique free parameter of the model, which controls the density at which the  $\Lambda\Lambda$  term changes its sign. As such we show that the bond energy controls the low density part of the EoS solely. This means that hypernuclear data cannot be used to determine the high density behavior of hyperonic matter, and other constraints from neutron star physics or heavy ion data are needed in that region. This general conclusion is certainly independent of our model and shall be found also in other approaches.

In the second step, the hypernuclear chart for even-even hypernuclei with  $Z \leq 120$  and  $\Lambda=2, 8, 20, 40,$  and  $70$  has been calculated using the Hartree-Fock method with Skyrme NN functional and designed  $\text{N}\Lambda$  and  $\Lambda\Lambda$  functionals. Six  $(\text{N}\Lambda + \Lambda\Lambda)$  functionals were used, optimized such as to reproduce the present experimental constraint of a bond energy of 1 MeV. The position of the hyperdriplines is determined with a 7% accuracy, with comparable contribution from the uncertainty on the NN functionals, and on the  $\Lambda$  related functionals. The number of such bound even-even hypernuclei is estimated to  $9770 \pm 429$ , leading to an estimation of the total number of hypernuclei with  $\Lambda < 70$  and  $Z < 120$  of  $491680 \pm 59000$ .

Significant deviations from Iron-Nickel elements can be found for hypernuclei with the largest binding energy per baryon, especially for  $\Lambda \geq 20$ . The spin-orbit weakening of the neutron magicity close to the neutron dripline is quenched the presence of hyperons. The nucleonic core profile is not much affected by the presence of hyperons, allowing for the persistence of the proton bubble in  $^{34}\text{Si}$  with additional hyperons.

The present results shall benefit from the more and more accurate design of the  $\Lambda$ -based functionals. The measurements of  $\Lambda$  and multi- $\Lambda$  hypernuclei, as well as  $\Lambda$ -density profiles, would greatly help to provide such critical information.

## ACKNOWLEDGMENTS

The authors thank I. Vidaña for fruitful discussions. This work has been partially funded by the SN2NS project ANR-10-BLAN-0503 and it has been supported by New-Compstar, COST Action MP1304 and the Institut Universitaire de France.



### Appendix A: Relation between the bond energy and the functional

For a nucleus hereafter called  $(A-1)$ , including one  $\Lambda$  and  $A-2$  nucleons, its total energy can be approximatively given by:

$$E_{\Lambda}^{(A-1)Z} \approx E^{(A-2)Z} + e_{\Lambda}(A-1), \quad (\text{A1})$$

where  $e_{\Lambda}(A-1)$  is the single particle energy of the  $\Lambda$  state in the  ${}_{\Lambda}^{A-1}Z$  hypernucleus, taking into account only the  $N\Lambda$  interaction. For the double- $\Lambda$   ${}_{\Lambda\Lambda}^AZ$  hypernucleus, we have also

$$E_{\Lambda\Lambda}^{(A)Z} \approx E^{(A-2)Z} + 2e_{\Lambda}(A) + U_{\Lambda}^{(\Lambda)}(\rho_{\Lambda}(A)), \quad (\text{A2})$$

where  $U_{\Lambda}^{(\Lambda)}(\rho_{\Lambda}(A))$  is the  $\Lambda$  potential term induced by the presence of  $\Lambda$  particles. In the present functional approach, we remind that the momentum dependence of the  $\Lambda\Lambda$  interaction is neglected, and that  $U_{\Lambda}^{(\Lambda)}$  is momentum independent. Using the local density approximation, it is a function of the average  $\Lambda$ -density in the  ${}_{\Lambda\Lambda}^AZ$  hypernucleus,  $\rho_{\Lambda}(A)$ . From the BHF framework, it can be shown that [13]

$$\varepsilon_{\Lambda\Lambda} = \frac{1}{2}\rho_{\Lambda}U_{\Lambda}^{(\Lambda)}. \quad (\text{A3})$$

Injecting Eqs. (A1) and (A2) into (16), the bond energy reads,

$$\Delta B_{\Lambda\Lambda}(A) \approx 2e_{\Lambda}(A-1) - 2e_{\Lambda}(A) - U_{\Lambda}^{(\Lambda)}(\rho_{\Lambda}(A)) \quad (\text{A4})$$

It should be noted that, in order to obtain Eq. (A4), we have assumed the independent particle approximation. Since the momentum dependence of  $U_{\Lambda}^{(\Lambda)}$  is neglected, the  $\Lambda$ -effective mass is the same in double- $\Lambda$  and single- $\Lambda$  hypernuclei, and depend only on  $\rho_N$  as in Eq. (34). The difference  $e_{\Lambda}(A-1) - e_{\Lambda}(A)$ , which is mostly induced by the rearrangement term in the mean field, is calculated to be small. We therefore approximate  $e_{\Lambda}(A-1) \approx e_{\Lambda}(A)$  to obtain

$$\Delta B_{\Lambda\Lambda}(A) \approx -U_{\Lambda}^{(\Lambda)}(\rho_{\Lambda}(A)) = -2\frac{\varepsilon_{\Lambda\Lambda}(\rho_{\Lambda}(A))}{\rho_{\Lambda}(A)}, \quad (\text{A5})$$

where Eq. (A3) has been used.

### Appendix B: Strangeness Analog Resonances

Strangeness analog resonances (SAR) are similar to isobaric analog states, with the transformation of a nucleon into an hyperon instead of a transformation of e.g. a neutron into a proton. In Ref. [43], Kerman and Lipkin studied the SAR states between nuclei and excited states of single hyperon hypernuclei. It is interesting to generalise this approach to multi- $\Lambda$  systems.

Kerman and Lipkin assumed that the energy difference (the degeneracy raising) between a nucleus and the corresponding hypernucleus state where a neutron is replaced by an hyperon, is due to i) the mass difference between the  $\Lambda$  and the neutron and ii) the difference between the nucleonic and the hyperonic potentials [43]:

$$\Delta E(\text{SAR}) \equiv m({}^AX_{\Lambda}^*) - m({}^AX) = (V_{0\Lambda} - V_{0n}) + (m_{\Lambda} - m_n) \quad (\text{B1})$$

where  $V_{0\Lambda}$  and  $V_{0n}$  are the depth of the hyperon and nucleons potentials, respectively, and  $\Lambda=1$  here.

This corresponds to an excitation energy in the hypernucleus of

$$E^* \equiv m({}^AX_{\Lambda}^*) - m({}^AX_{\Lambda}) = -S_n({}^AX) + (V_{0\Lambda} - V_{0n}) + B_{\Lambda} \quad (\text{B2})$$

where  $B_{\Lambda}$  is the binding energy of the hyperon in the single  $\Lambda$  hypernucleus and  $S_n({}^AX)$  the one neutron separation energy of the  ${}^AX$  nucleus.

The questions arises whether the above relation can be generalised to multi- $\Lambda$  nuclei. A straightforward derivation allows to derive the mass (namely the excited state) of the hypernucleus having  $\Lambda$  hyperons from the mass of the initial nucleus:

$$\Delta E(\text{SAR}) = \Lambda[(V_{0\Lambda} - V_{0n}) + (m_{\Lambda} - m_n)] \quad (\text{B3})$$

where  $\Lambda \geq 1$ . It should be noted that the  $\Lambda\Lambda$  interaction is neglected here, as well as rearrangement terms. This could result in a significant different form of Eq. (B3). However, as shown below, the energy position of SAR states will mainly be impacted by the nucleon vs.  $\Lambda$  mass difference.

Eq. (B3) shows that the SAR states in multihyperons are expected to display a rather harmonic spectrum, since the last term in brackets of the right-hand-side remains rather constant: there is about 30 MeV difference between the neutron and the hyperon mean potentials [12], and 170 MeV difference between the neutron and the hyperon masses:

$$m({}^AX_{\Lambda}^*) \simeq m({}^AX) + \Lambda.200\text{MeV} \quad (\text{B4})$$

It should be noted that this 200 MeV constant value originates from the saturation properties in hypernuclei, which in turn leads to a constant difference between the nucleon and the hyperon potentials. Moreover, in the corresponding hypernuclei, these states would correspond to excited states located around  $\Lambda.30$  MeV, which becomes unbound already for small value of  $\Lambda$ . In summary, the SAR states have been generalised to multi-hyperons hypernuclei. They shall not correspond to bound states for most of them, but to resonances embedded in the continuum.

- Phys. E Vol. 23, 1450052 (2014).
- [3] H.Y. Sang, X.S. Wang, J.H. Wang and H.F. Lü, *Eur. Phys. J. A* 50, 52 (2014).
- [4] W. Greiner, *Lecture notes in Physics* 581, J.M. Arias and M. Lozano (Eds.), Springer-Verlag, (2001).
- [5] C. Samanta, P. Roy Chowdhury and D.N. Basu, *J. Phys. G* 32, 363 (2006).
- [6] M. Rufa, J. Schaffner, J. Maruhn, H. Stöcker, W. Greiner, and P.-G. Reinhard, *Phys. Rev. C* 42, 2469 (1990).
- [7] J. Schaffner, C. Greiner, and H. Stöcker, *Phys. Rev. C* 46, 322 (1992).
- [8] J. Mares, J. Zofka, *Z. Phys.* 345, 47 (1993).
- [9] J. Schaffner, C.B. Dover, A. Gal, et al., *Ann. Phys.* 235, 35 (1994).
- [10] D.E. Lansky, Y. Yamamoto, *Phys. Rev. C* 55, 2330 (1997).
- [11] D.E. Lansky, *Phys. Rev. C* 58, 3351 (1998).
- [12] J. Cugnon, A. Lejeune, H.-J. Schulze, *Phys. Rev. C* 62, 064308 (2000).
- [13] I. Vidaña, A. Polls, A. Ramos, and H.-J. Schulze, *Phys. Rev. C* 64, 044301 (2001).
- [14] J. Meng, H. Toki, S.G. Zhou, et al., *Prog. Part. Nucl. Phys.* 57, 470 (2006).
- [15] Xian-Rong Zhou, H.-J. Schulze, H. Sagawa, Chen-Xu Wu, and En-Guang Zhao, *Phys. Rev. C* 76, 034312 (2007).
- [16] H.F. Lü, *Chin. Phys. Lett.* 25, 3613 (2008).
- [17] N. Guleria, S.K. Dhiman, R. Shyam, *Nucl. Phys. A* 886, 71 (2012).
- [18] F. Minato and K. Hagino, *Phys. Rev. C* 85, 024316 (2012).
- [19] J. Erler, N. Birge, M. Kortelainen, W. Nazarewicz, E. Olsen, A.M. Perhac, M. Stoitsov, *Nature* 486, 509 (2012).
- [20] P.-G. Reinhard and W. Nazarewicz, *Phys. Rev. C* 87, 014324 (2013).
- [21] Wei-Chia Chen and J. Piekarewicz *Phys. Rev. C* 90, 044305 (2014).
- [22] P. Finelli, N. Kaiser, D. Vretenar and W. Weise, *Phys. Lett. B* 658, 90 (2007); *Nucl. Phys. A* 831, 163 (2009).
- [23] E. Chabanat, P. Bonche, P. Haensel, J. Meyer and R. Schaeffer, *Nucl. Phys. A* 635, 231 (1998).
- [24] H.-J. Schulze and T. Rijken, *Phys. Rev. C* 88, 024322 (2013).
- [25] P.M.M. Maessen, T.A. Rijken and J.J. de Swart, *Phys. Rev. C* 40, 2226 (1989).
- [26] T.A. Rijken, V.G.J. Stoks and Y. Yamamoto, *Phys. Rev. C* 59, 21 (1999).
- [27] V.G.J. Stoks and T.A. Rijken, *Phys. Rev. C* 59, 3009 (1999).
- [28] J. Bartel, K. Bencheikh and J. Meyer, *Phys. Rev. C* 77, 024311 (2008).
- [29] M. Bender, P.-H. Heenen, P.-G. Reinhard, *Rev. Mod. Phys.* 75, 121-180 (2003).
- [30] P.B. Demorest, T. Pennucci, S.M. Ransom, M.S.E. Roberts and J.W.T. Hessels, *Nature* 467, 1081 (2010).
- [31] E.N.E. Van Dalen, G. Colucci, G., & A. D. Sedrakian, *Physics Letters B* 734, 383 (2014).
- [32] G. Colucci and A. Sedrakian *Phys. Rev. C* 87, 055806 (2013)
- [33] G.B. Franklin, *Nucl. Phys. A* 585, 83c (1995).
- [34] S. Aoki, et al., *Nucl. Phys. A* 828, 191 (2009).
- [35] J.K. Ahn, et al., *Phys. Rev. C* 88, 014003, (2013).
- [36] O. Hashimoto and H. Tamura, *Prog. Part. Nucl. Phys.* 57, 564 (2006), and references therein.
- [37] M.-G. Porquet and O. Sorlin, *Prog. Part. and Nucl. Phys.* 61, 602 (2008).
- [38] J. Dobaczewski, I. Hamamoto, W. Nazarewicz, and J. A. Sheikh, *Phys. Rev. Lett.* 72, 981 (1994).
- [39] D. Peña Arteaga, E. Khan, and P. Ring, *Phys. Rev. C* 79, 034311 (2009).
- [40] K. Tanida, H. Tamura, D. Abe, H. Akikawa, K. Araki, H. Bhang, T. Endo, Y. Fujii, T. Fukuda, O. Hashimoto, K. Imai, H. Hotchi, Y. Kakiguchi, J.H. Kim, Y. D. Kim, T. Miyoshi, T. Murakami, T. Nagae, H. Noumi, H. Outa, K. Ozawa, T. Saito, J. Sasao, Y. Sato, S. Satoh, R.I. Sawafta, M. Sekimoto, T. Takahashi, L. Tang, H.H. Xia, S.H. Zhou, and L.H. Zhu, *Phys. Rev. Lett.* 86, 1982 (2001), and refs. therein.
- [41] E. Khan, M. Grasso, J. Margueron, and N. Van Giai, *Nucl. Phys. A* 800, 37 (2008).
- [42] M. Grasso, L. Gaudefroy, E. Khan, T. Nikšić, J. Piekarewicz, O. Sorlin, N. Van Giai, and D. Vretenar, *Phys. Rev. C* 79, 034318 (2009).
- [43] A.K. Kerman and H.J. Lipkin, *Ann. Phys.* 66, 738 (1971).